Research in Astronomy and Astrophysics, 24:065008 (13pp), 2024 June https://doi.org/10.1088/1674-4527/ad3b3c

Study of Complex Nitrogen and Oxygen-bearing Molecules toward the High-mass Protostar IRAS 18089–1732

Arijit Manna[1], Sabyasachi Pal[1], Tapas Baug[2], and Sougata Mondal[1]
[1] Department of Physics, Midnapore City College, Paschim Medinipur, West Bengal, 721129, India; arijitmanna@mcconline.org.in
[2] S. N. Bose National Centre for Basic Sciences, Block-JD, Sector-III, Salt Lake City, Kolkata, 700106 India; sabya.pal@gmail.com
Received 2024 January 18; revised 2024 April 3; accepted 2024 April 3; published 2024 May 20

Abstract

The observation of oxygen (O)- and nitrogen (N)-bearing molecules gives an idea about the complex prebiotic chemistry in the interstellar medium. Recent millimeter and submillimeter wavelength observations have shown the presence of complex O- and N-bearing molecules in the star formation regions. So, the investigation of those molecules is crucial to understanding the chemical complexity in the star-forming regions. In this article, we present the identification of the rotational emission lines of N-bearing molecules ethyl cyanide (C_2H_5CN) and cyanoacetylene (HC_3N), and O-bearing molecule methyl formate (CH_3OCHO) toward high-mass protostar IRAS 18089–1732 using the Atacama Compact Array. We also detected the emission lines of both the N- and O-bearing molecule formamide (NH_2CHO) in the envelope of IRAS 18089–1732. We have detected the $v = 0$ and 1 state rotational emission lines of CH_3OCHO. We also detected the two vibrationally excited states of HC_3N ($v7 = 1$ and $v7 = 2$). The estimated fractional abundances of C_2H_5CN, HC_3N ($v7 = 1$), HC_3N ($v7 = 2$), and NH_2CHO toward IRAS 18089–1732 are $(1.40 \pm 0.5) \times 10^{-10}$, $(7.5 \pm 0.7) \times 10^{-11}$, $(3.1 \pm 0.4) \times 10^{-11}$, and $(6.25 \pm 0.82) \times 10^{-11}$ respectively. Similarly, the estimated fractional abundances of CH_3OCHO ($v = 0$) and CH_3OCHO ($v = 1$) are $(1.90 \pm 0.9) \times 10^{-9}$ and $(8.90 \pm 0.8) \times 10^{-10}$, respectively. We also created the integrated emission maps of the detected molecules, and the observed molecules may have originated from the extended envelope of the protostar. We show that C_2H_5CN and HC_3N are most probably formed via the subsequential hydrogenation of the CH_2CHCN and the reaction between C_2H_2 and CN on the grain surface of IRAS 18089–1732. We found that NH_2CHO is probably produced due to the reaction between NH_2 and H_2CO in the gas phase. Similarly, CH_3OCHO is possibly created via the reaction between radical CH_3O and radical HCO on the grain surface of IRAS 18089–1732.

Key words: ISM: individual objects (IRA 18089–1732) (except) – ISM: abundances – ISM: kinematics and dynamics – stars: formation – astrochemistry

1. Introduction

The study of complex organic molecules (COMs) from massive stars ($M > 8\,M_\odot$) is important for understanding the chemical complexity in the interstellar medium (ISM; van Dishoeck & Blake 1998; Herbst & van Dishoeck 2009). High-mass stars generate a significant amount of heavy atomic elements, produce large amounts of ultraviolet (UV) radiation, and inject turbulent energy into the ISM (Zapata et al. 2006). High-mass protostars are located in a rich cluster environment, and it is challenging to understand the physical and chemical formation processes (de Wit et al. 2005). High-mass protostars are highly luminous ($\geqslant 10^3\,L_\odot$), and these sources are deeply embedded in massive envelopes that contain a high gas temperature ($\geqslant 100$ K) and gas density above $10^6\,\mathrm{cm}^{-3}$ (Liu et al. 2021). The study of the physical phenomena of high-mass protostellar disks is a major concern in high-mass star-forming regions. Over the past few years, indirect evidence for the existence of massive disks has accumulated, but there is still no clear proof of massive disks. Additionally, there are several methods for directly studying massive disks. Infrared and millimeter-wavelength continuum observations have revealed several attractive disk candidates, but they are unable to provide kinematic proof of potential accretion disks owing to a lack of velocity information (Shepherd et al. 2000; Chini et al. 2004). On the other hand, class II methanol (CH_3OH) and water (H_2O) maser emission found kinematic signatures from the massive disk candidates, but since maser emission is extremely selective and demands specific conditions, such studies do not permit more statistical analysis of massive disk properties (Torrelles et al. 1996; Pestalozzi et al. 2004). The most likely method to find and investigate disks in high-mass star formations is to detect thermal molecular line emissions, which are predicted to be sensitive to the gas properties and kinematics of the disks. Therefore, spectral line surveys in the millimeter and submillimeter wavelengths are crucial for understanding molecular gas properties, such as column

density and excitation temperature. The best method is to search the rotational emission lines of acetonitrile (CH_3CN) and methyl acetylene (CH_3CCH) because both molecules are known as gas thermometers for interstellar gas in massive protostars, hot molecular cores, and hot corinos (Andron et al. 2018). The prebiotic chemistry of high- and low-mass protostellar candidates may be the same, and a detailed analysis of the chemical evolution of high- and low-mass protostellar sources is not only important for astrochemistry but also crucial for understanding the process of star formation. Over the past decade, a variety of COMs have been discovered in protostellar cores on the scale of a few thousand astronomical units (Sakai & Yamamoto 2013). Two different scenarios were identified: (1) prebiotic chemistry in hot corinos, which is characterized by the richness of saturated COMs (Cazaux et al. 2003; Herbst & van Dishoeck 2009; Caselli & Ceccarelli 2012), and (2) warm carbon chain chemistry, which is characterized by the richness of unsaturated hydrocarbons (Sakai et al. 2008). Studying the chemical evolution of protostellar sources requires the study of isolated sources that are unaffected by nearby protostellar feedback. Isolated protostellar sources are excellent laboratories for theories of both chemical evolution and star formation (Evans et al. 2015).

Most chemical models of protostellar sources and hot molecular cores utilize grain surface chemistry to produce different types of complex organic compounds (Tielens & Charnley 1997; Garrod 2013; Manna & Pal 2024). The hydrogenation of solid oxygen (O), carbon (C), nitrogen (N), and carbon monoxide (CO) in the cold ($\leqslant$20 K) prestellar phase produces CH_3OH and other hydrogenated species such as H_2O, NH_3, and CH_4 (Tielens & Hagen 1982). UV radiation photodissociates these surface ices, and when the cloud core heats up during the protostellar phase, the fragments become mobile. Consequently, complex molecules are formed during the subsequent recombination of the photofragments and evaporate when the grain temperature increases above the ice sublimation temperature of $\geqslant$100 K (Garrod & Herbst 2006; Garrod et al. 2008; Manna & Pal 2024). For example, CH_3OCH_3, CH_3OCHO, and C_2H_5OH are formed by UV processing of CH_3OH ice (Öberg et al. 2009). Finally, the hot-core gas phase chemistry between evaporated molecules may cause second-generation species to become more complex (Millar et al. 1991; Charnley et al. 1992). One of the most significant impacts of an equatorial rather than a spherical structure is that UV light may more easily exit from the central source and illuminate the surface layers of the surrounding disk or toroid, as well as the larger-scale envelope (Bruderer et al. 2009, 2010; Isokoski et al. 2013) (Figure 2). This can result in ice-producing COMs that are faster than CH_3OH. Another effect of UV radiation is enhanced photodissociation of gaseous N_2 and CO. Consequently, more atomic N and C are easily accessible for grain surface chemistry, which might result in an increased abundance of species such as HNCO and NH_2CHO (Garrod 2013).

IRAS 18089–1732 (hereafter IRAS 18089) is a well-known high-mass protostar that contains an ultra-compact (UC) H II region (Liu et al. 2021). That source is located at a distance of 2.34 kpc from the Earth (Xu et al. 2011). The luminosity and gaseous mass of IRAS 18089 are 1.3×10^4 $L_\odot$ and 1000 $M_\odot$ respectively, which are estimated from the single-dish millimeter wavelength continuum emission (Beuther et al. 2002a; Sridharan et al. 2002). Earlier, the emission lines of CH_3OH, SO, SO_2, H_2S, and many other COMs were detected toward IRAS 18089, but no column densities or abundances were reported (Beuther et al. 2004b; Isokoski et al. 2013). Earlier estimated excitation temperature of CH_3CN ($\sim$350 K) toward IRAS 18089 indicated that the source is deeply embedded in the hot core (Beuther et al. 2004b). The molecular outflow of SiO ($J = 5$–4) is also evident toward IRAS 18089, which was detected using the Submillimeter Array (SMA; Beuther et al. 2004b). Additionally, the Goldreich-Kylafis effect was observed for the CO ($J = 3$–2) emission line, which revealed a linear polarization fraction of up to 8% (Beuther et al. 2010). The H_2O and CH_3OH maser emissions were also detected toward IRAS 18089 (Beuther et al. 2002b). Recently, Qin et al. (2022) conducted a spectral line survey of the rotational emission lines of ethyl cyanide (C_2H_5CN), methyl formate (CH_3OCHO), and methanol (CH_3OH) toward 146 high-mass star-forming regions using the ATOMS survey data (Liu et al. 2020). Qin et al. (2022) mentioned the detection of only two and six transition lines of C_2H_5CN and CH_3OCHO toward IRAS 18089 among which one transition line of C_2H_5CN and two transition lines of CH_3OCHO are blended with other molecules (see supplementary data of Qin et al. 2022). Qin et al. (2022) also do not discuss the abundance and proper gas phase and grain surface chemistry of those molecules toward IRAS 18089. This indicates that another detailed molecular spectral line study is needed to understand the abundance and prebiotic chemistry of different COMs toward IRAS 18089.

In this paper, we present the detection of rotational emission lines of C_2H_5CN, CH_3OCHO, HC_3N, and NH_2CHO toward IRAS 18089. The chemical diagram of those molecules is created using the molecular modeling software `Avogadro` (Hanwell et al. 2012), as shown in Figure 1. Previously, the emission lines of C_2H_5CN, CH_3OCHO, HC_3N, and NH_2CHO were detected toward hot molecular cores G10.47+0.03 (Gorai & Bhat et al. 2020; Mondal et al. 2021; Manna & Pal 2023; Mondal et al. 2023), G31.41+0.31 (Mininni et al. 2023), Orion KL (Beuther et al. 2005), Sgr B2 (N) (Belloche et al. 2013), and low-mass protostar IRAS 16293-2422 (Jørgensen et al. 2016; Calcutt et al. 2018). The paper is organized in the following manner. The observations and data reduction are presented in Section 2. The result of the detection of emission lines of complex molecules is shown in Section 3. The

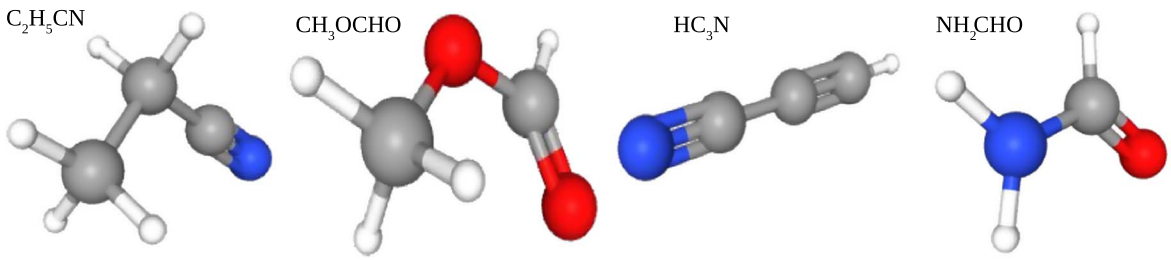

Figure 1. Three-dimensional molecular structure of C_2H_5CN, CH_3OCHO, HC_3N, and NH_2CHO. The gray atoms are carbon (C), the red atoms are oxygen (O), the white atoms are hydrogen (H), and the blue atoms are nitrogen (N).

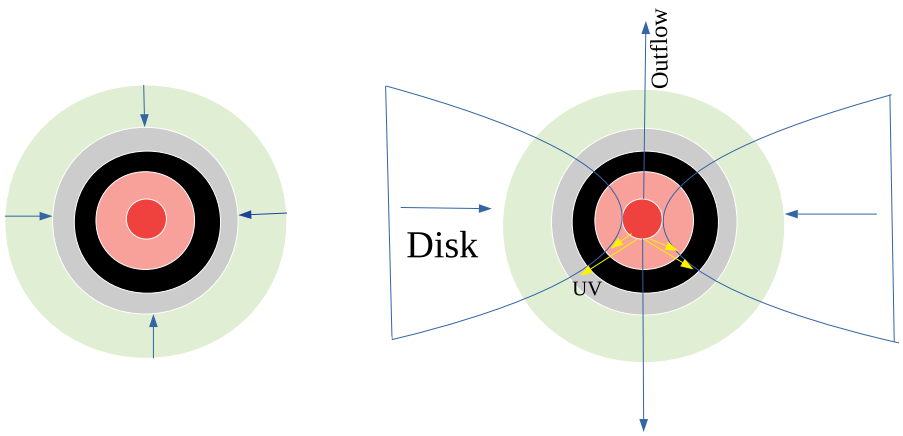

Figure 2. A cartoon diagram of a high-mass protostar with a spherical shape (left) and a protostar with a flattened disk-like structure (right), with increasing UV photons illuminating the walls of the outflow cavity.

Table 1
Observation Summary of IRAS 18089

Observation Date (yyyy-mm-dd)	Integration Time (s)	Frequency Range (GHz)	Spectral Resolution (kHz)	Sensitivity (10 km s^{-1}) (mJy $beam^{-1}$)	Field of View (FOV) (″)
2017-09-18	5624.64	127.49–128.48	488.28	5.91	74.23
…	…	129.75–130.75	488.28	5.37	…
…	…	139.09–140.09	488.28	5.15	…
…	…	140.45–141.45	488.28	5.01	…

discussion and conclusion of the detection of complex molecules are featured in Sections 4 and 5 respectively.

2. Observations and Data Reductions

We used the cycle 4 archival data of IRAS 18089, observed employing the 7 m Atacama Compact Array (ACA) of the Atacama Large Millimeter/submillimeter Array (ALMA) (ID: 2016.2.00005.S. PI: Rivilla, Victor). The observations were performed in Band 4 (frequency range 127.49–141.45 GHz). The observed phase center of IRAS 18089 was $(\alpha, \delta)_{J2000} =$ 18:11:51.400, −17:31:28.00. The observation was carried out on 2017 September 18, using eight antennas. The observations were recorded in spectral ranges 127.49–128.48 GHz, 129.75–130.75 GHz, 139.09–140.09 GHz, and 140.45–141.45 GHz, with a corresponding spectral resolution of 488 kHz. During the observation of IRAS 18089, the flux calibrator and bandpass calibrator were J1924–2914, and the phase calibrator was taken as J1833–210B. The observation summary is shown in Table 1.

We used the Common Astronomy Software Application (CASA 5.4.1) with the data reduction automated pipeline for data reduction and spectral imaging of IRAS 18089 (McMullin et al. 2007). For flux calibration of IRAS 18089, we used the

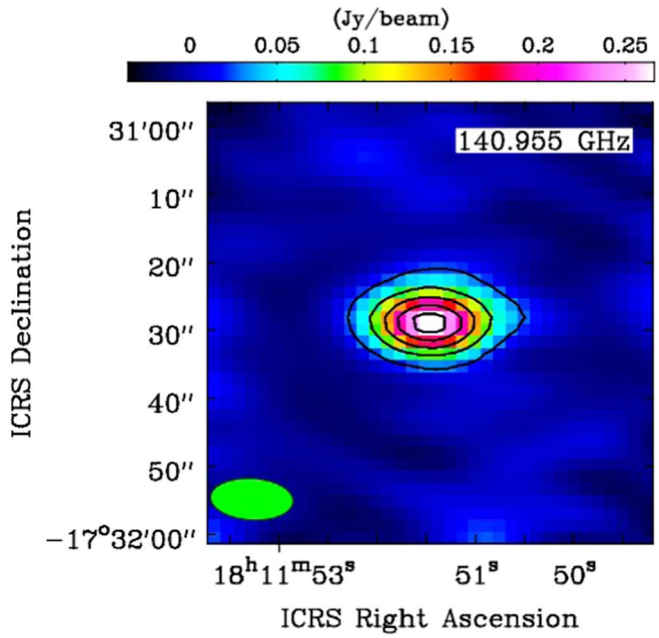

Figure 3. The 2.1 mm continuum map of IRAS 18089 overlaid with black contours. The contour levels start at 3σ, where σ is the rms (26.63 mJy beam^{-1}) of the continuum image. The contour levels increase by a factor of $\sqrt{2}$. The green circle indicates the synthesized beam of the continuum image.

Perley–Butler 2017 flux calibrator model for each baseline to scale the continuum flux density of the flux calibrator using the CASA task `SETJY` with 5% accuracy (Perley & Butler 2017). Executing the CASA pipeline tasks `hifa bandpassflag` and `hifa flagdata`, we create the flux and bandpass calibration after flagging the defective channels and antenna data. After the initial data reduction, we used the CASA task `MSTRANSFORM` with all available rest frequencies to separate the target data of IRAS 18089. We produced the continuum emission maps of IRAS 18089 for line-free channels using the CASA task `TCLEAN` with `HOGBOM` deconvolver. After the production of the continuum images, we used the task `UVCONTSUB` in the UV plane of separated calibrated data of IRAS 18089 for the continuum subtraction. To create the spectral images of IRAS 18089, we utilized the CASA task `TCLEAN` with `SPECMODE=CUBE` parameter and Briggs weighting robust value of 0.5. Both the continuum map and spectral cube were corrected for the primary beam using the CASA `IMPBCOR` task.

3. Result

3.1. Dust Continuum Emission

The 2.1 mm dust continuum image of IRAS 18089 is depicted in Figure 3. We employ the CASA `IMFIT` task to estimate parameters of the central core, such as integrated flux density, peak flux density, corresponding position angle, and rms noise level. The estimated peak flux density and integrated flux density of the source are 274.9 ± 6.5 mJy beam^{-1} and 346.1 ± 14 mJy, respectively, with an rms noise of 26.63 mJy beam^{-1}. The deconvolved source size is $5\farcs14 \times 3\farcs59$ at a position angle of $89\fdg8$. The synthesized beam size of the continuum image is $12\farcs78 \times 7\farcs20$. Thus, the continuum core is not resolved in the IRAS 18089 region.

3.1.1. Estimation of Hydrogen (H_2) Column Density

For optically thin dust continuum emission, the peak flux density (S_ν) can be expressed as

$$S_\nu = B_\nu(T_d)\tau_\nu\Omega_{\rm beam} \text{ (Gorai et al. 2020)}, \quad (1)$$

where $B_\nu(T_d)$ represents the Planck function at dust temperature T_d (Whittet 1992), τ_ν indicates the optical depth, and $\Omega_{\rm beam} = (\pi/4\ln 2) \times \theta_{\rm major} \times \theta_{\rm minor}$ signifies the solid angle of the synthesized beam. The equation of optical depth in terms of the mass density of dust can be written as,

$$\tau_\nu = \rho_d\kappa_\nu L \text{ (Gorai et al. 2020)}, \quad (2)$$

where ρ_d represents the mass density of dust, κ_ν is the mass absorption coefficient, and L defines the path length. The mass density of the dust can be expressed in terms of the dust-to-gas mass ratio (Z),

$$\rho_d = Z\mu_{\rm H}\rho_{\rm H_2} = Z\mu_{\rm H}N_{\rm H_2}2m_{\rm H}/L \text{ (Gorai et al. 2020)}, \quad (3)$$

where $\mu_{\rm H}$ defines the mean atomic mass per hydrogen, $\rho_{\rm H_2}$ is the hydrogen mass density, $m_{\rm H}$ represents the mass of hydrogen, and $N_{\rm H_2}$ is the column density of molecular hydrogen. We take the dust temperature $T_d = 30$ K (Sanhueza et al. 2021), $\mu_{\rm H} = 1.41$, and $Z = 0.01$ (Cox & Pilachowski 2000). The estimated peak flux density of the dust continuum of IRAS 18089 at frequency 140.955 GHz is 274.9 ± 6.5 mJy beam^{-1}. From Equations (1), (2), and (3), the column density of molecular hydrogen can be expressed as,

$$N_{\rm H_2} = \frac{S_\nu/\Omega}{2\kappa_\nu B_\nu(T_d)Z\mu_{\rm H}m_{\rm H}} \text{ (Gorai et al. 2020)}. \quad (4)$$

For estimation of the mass absorption coefficient (κ_ν), we adopt the formula $\kappa_\nu = 0.90(\nu/230\,{\rm GHz})^\beta\,{\rm cm^2\,g^{-1}}$ (Motogi et al. 2019), where $k_{230} = 0.90\,{\rm cm^2\ g^{-1}}$ indicates the emissivity of the dust grains at a gas density of $10^6\,{\rm cm^{-3}}$, which is covered by a thin ice mantle at 230 GHz. The dust spectral index (β) of $\sim$1.6 toward IRAS 18089 is adopted from Sanhueza et al. (2021). Using the mass absorption coefficient formula, the estimated value of κ_ν is 0.411. Using Equation (4), we estimate the column density of the molecular hydrogen (N_{H_2}) toward IRAS 18089 to be $(8.01 \pm 0.4) \times 10^{23}\,{\rm cm^{-2}}$. The earlier estimated column density of molecular H_2 toward IRAS 18089 at wavelength 1.2 mm using the SMA is $9.5 \times 10^{23}\,{\rm cm^{-2}}$ (Beuther et al. 2005), which is quite similar to our derived column density of H_2 ($(8.01 \pm 0.4) \times 10^{23}\,{\rm cm^{-2}}$) using the ACA at wavelength 2.1 mm.

3.2. Spectral Line Analysis of IRAS 18089

We extracted the molecular spectrum of the high-mass protostar IRAS 18089 for a 20″.2 diameter circular region centered at $(\alpha,\ \delta)_{J2000} = 18{:}11{:}51.400,\ -17{:}31{:}28.00$. The synthesized beam sizes of the spectral images of IRAS 18089 at frequency ranges of 127.49–128.48 GHz, 129.75–130.75 GHz, 139.09–140.09 GHz, and 140.45–141.45 GHz are 12″.82 × 6″.40, 12″.90 × 6″.32, 12″.66 × 6″.02, and 12″.18 × 6″.09 respectively. The systemic velocity (V_{LSR}) of IRAS 18089 is 33.8 km s^{-1} (Beuther et al. 2005). For identification of the emission line of COMs in the spectra, we use local thermodynamic equilibrium (LTE) model spectra with the Cologne Database for Molecular Spectroscopy (CDMS) molecular database (Müller et al. 2005). For LTE analysis, we use the LTE-RADEX module in CASSIS (Vastel et al. 2015). The LTE assumption is valid in this case as the gas density of the warm inner region of the target is 1.3×10^7 cm^{-3} (Sanhueza et al. 2021). The identification of the different types of COMs is discussed below.

3.2.1. Ethyl Cyanide (C_2H_5CN)

We detected a total of four rotational emission lines of the complex N-bearing molecule C_2H_5CN toward IRAS 18089 using the LTE-modeled spectra. The upper-state energies (E_u) of the detected emission lines of C_2H_5CN vary between 47.23 and 57.48 K. A Gaussian fit to the observed spectra of C_2H_5CN was performed to estimate the proper FWHM in km s^{-1} and integrated intensity ($\int T_{mb} dV$) in K km s^{-1}. The resultant LTE and Gaussian fitting of spectral lines of C_2H_5CN are displayed in Figure 4, and the corresponding spectral parameters are listed in Table 2. We also confirmed that the detected emission lines of C_2H_5CN are non-blended, and all detected emission lines of C_2H_5CN exhibit above 5σ significance. The best-fit column density of C_2H_5CN is $(1.13 \pm 0.4) \times 10^{14}$ cm^{-2} with an excitation temperature of 200 ± 54 K, which is obtained using the LTE modeling. The fractional abundance of C_2H_5CN toward IRAS 18089 with respect to H_2 is $(1.40 \pm 0.5) \times 10^{-10}$.

3.2.2. Methyl Formate (CH_3OCHO)

We identified a total of sixteen rotational emission lines of CH_3OCHO toward IRAS 18089 using the LTE model with more than 5σ significance level. The resultant LTE and Gaussian-fitted spectral profiles of CH_3OCHO are shown in Figure 4, and the spectral line parameters of CH_3OCHO are presented in Table 2. We observed the $V_t = 0$ and $V_t = 1$ states in the transitions of the CH_3OCHO. The $V_t = 0$ and $V_t = 1$ states correspond to the ground and first torsionally excited states of CH_3OCHO. We find that the upper state energies (E_u) of the detected emission lines of CH_3OCHO ($V_t = 0$) vary between 40.71 and 114.60 K. Similarly, the upper state energies (E_u) of the CH_3OCHO ($V_t = 1$) vary between 223.32 and 235.0 K. We also observe the torsional substates A and E in the transitions of CH_3OCHO due to the internal rotation of the methyl (CH_3) group. During the spectral fitting using the LTE model, we observed that the $J = 17(6,11)$–$17(5,12)$A transition line of CH_3OCHO ($V_t = 0$) is not fitted well because that emission line is blended with CH_3OCH_3. In Table 2, the transitions of CH_3OCHO are presented corresponding to $V_t = 0$ and $V_t = 1$ states. Using the LTE model, the best-fit column density of the CH_3OCHO $V_t = 0$ is $(1.5 \pm 0.3) \times 10^{15}$ cm^{-2} and $V_t = 1$ is $(7.1 \pm 0.5) \times 10^{14}$ cm^{-2} with corresponding excitation temperatures of 200 ± 48 K and 196 ± 74 K. The column density of CH_3OCHO varies between the $V_t = 0$ and $V_t = 1$ torsional excited states because the first torsional excited state ($V_t = 1$) of CH_3OCHO is located at about 132 cm^{-1} above the ground state ($V_t = 0$), where 1 cm^{-1} = 1.438 K (Tudorie et al. 2012). The estimated abundances of CH_3OCHO with respect to H_2 toward IRAS 18089 are $(1.90 \pm 0.9) \times 10^{-9}$ (for $V_t = 0$) and $(8.90 \pm 0.8) \times 10^{-10}$ (for $V_t = 1$).

3.2.3. Cyanoacetylene (HC_3N)

We detected two vibrationally excited states of HC_3N ($v7 = 1$ and $v7 = 2$) toward IRAS 18089. Using the LTE-modeled spectra, we identified two rotational emission lines of $v7 = 1$ state and three rotational emission lines of $v7 = 2$ states of HC_3N. The detected vibrationally excited HC_3N emission lines exhibit the higher upper-state energies of E_{up}/k ∼366.80–366.86 K (for $v7 = 1$) and ∼687.82–691.10 K (for $v7 = 2$). The higher vibrational states of HC_3N ($v7 = 1$ and $v7 = 2$) with higher upper state energies have the ability to trace the inner hot gas near the central star. The resultant detected spectral lines of HC_3N ($v7 = 1$ and $v7 = 2$) are shown in Figure 4, and the spectral line parameters of HC_3N ($v7 = 1$ and $v7 = 2$) are presented in Table 2. Using the LTE model, the best-fit column density of HC_3N with $v7 = 1$ and $v7 = 2$ excited states are $(6.02 \pm 0.5) \times 10^{13}$ cm^{-2} and $(2.50 \pm 0.3) \times 10^{13}$ cm^{-2} respectively, with excitation temperatures of 160 ± 25 K and 180 ± 20 K. The estimated fractional abundances of HC_3N toward IRAS 18089 are $(7.5 \pm 0.7) \times 10^{-11}$ (for $v7 = 1$) and $(3.1 \pm 0.4) \times 10^{-11}$ (for $v7 = 2$).

3.2.4. Formamide (NH_2CHO)

We have detected a single transition line of NH_2CHO toward IRAS 18089 using the LTE-modeled spectra. We detected the $J = 6(2,4)$–$5(2,3)$, $F = 6$–5 transition line of NH_2CHO. We do not observe any other transition lines of NH_2CHO in the entire data. The upper-state energy (E_u) of the detected emission line of NH_2CHO is 33.38 K. To estimate the proper FWHM in km s^{-1} and integrated intensity ($\int T_{mb} dV$) in K km s^{-1} of the emission line of NH_2CHO, we fitted the Gaussian model over the observed spectra of NH_2CHO. The resultant LTE and Gaussian fitting spectral lines of NH_2CHO are shown in Figure 4, and the corresponding spectral parameters are listed in Table 2. We observed that the detected emission lines of

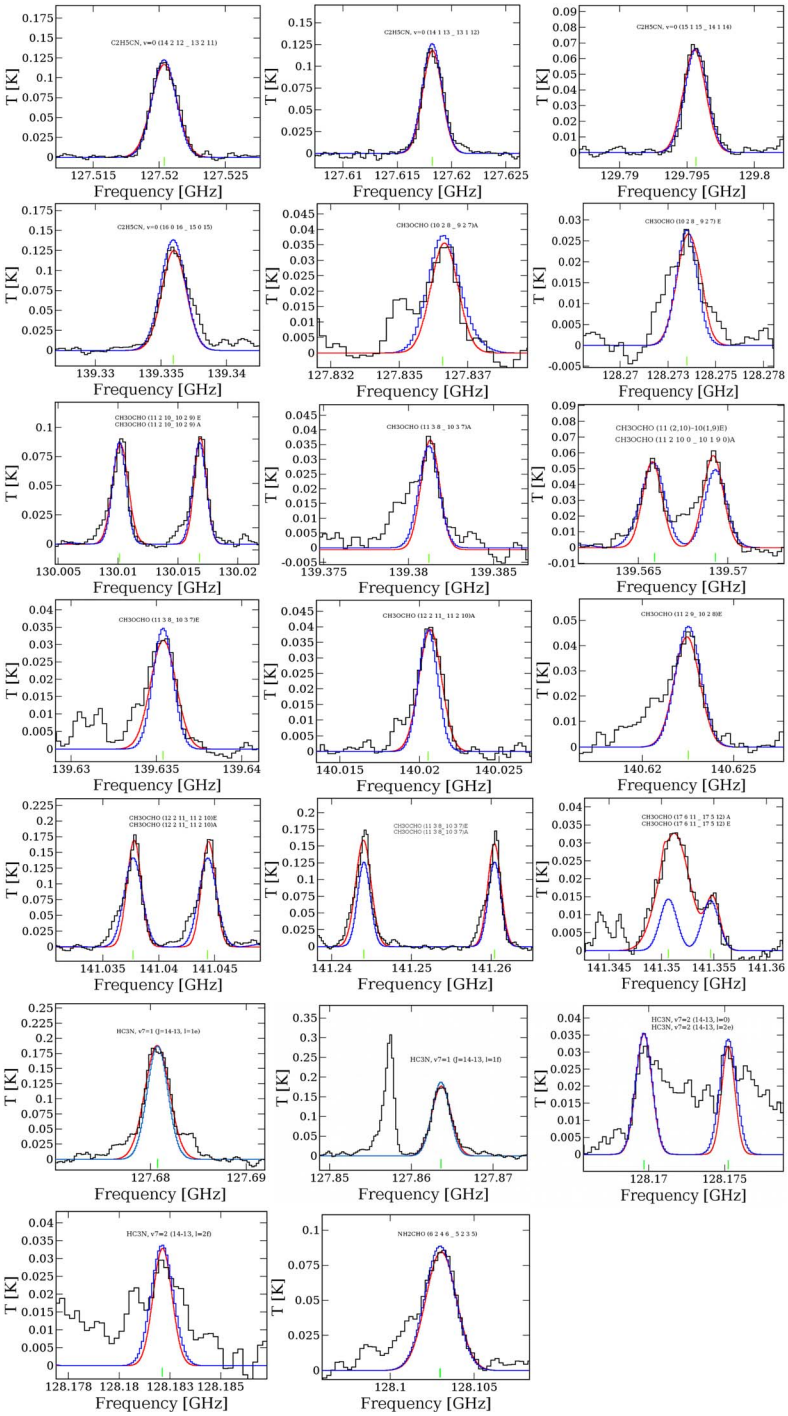

Figure 4. Rotational emission lines of C_2H_5CN, CH_3OCHO (both $V_t = 0$ and $V_t = 1$), HC_3N (both $v7 = 1$ and $v7 = 2$), and NH_2CHO toward IRAS 18089 with different transitions. The black lines present the observed millimeter-wavelength spectra of IRAS 18089 and the blue synthetic spectra correspond to the LTE model spectra of C_2H_5CN, CH_3OCHO ($V_t = 0$ and $V_t = 1$), HC_3N ($v7 = 1$ and $v7 = 2$), and NH_2CHO. The red spectrum indicates the Gaussian model which is fitted over the detected molecular spectra. The green vertical lines indicate the rest frequency positions of the detected transitions of C_2H_5CN, CH_3OCHO (both $V_t = 0$ and $V_t = 1$), HC_3N (both $v7 = 1$ and $v7 = 2$), and NH_2CHO.

Table 2
Summary of the Line Properties of the Detected Molecules toward IRAS 18089

Molecule	Observed Frequency[a] (GHz)	Transition[a]	E_u[a] (K)	A_{ij}[a] (s^{-1})	FWHM[b] (km s^{-1})	$\int T_{mb} dV$[b] (K km s^{-1})	Column Density (cm^{-2})	Excitation Temperature (K)	Remark[c]
C_2H_5CN	127.520	14(2,12)–13(2,11)	50.02	1.69×10^{-4}	5.52 ± 0.24	0.587			Non blended
	127.618	14(1,13)–13(1,12)	47.23	1.72×10^{-4}	5.16 ± 0.28	0.563	$(1.13 \pm 0.4) \times 10^{14}$ cm^{-2}	200 ± 54 K	Non blended
	129.795	15(1,15)–14(1,14)	51.09	1.82×10^{-4}	4.82 ± 0.64	0.255			Non blended
	139.335	16(0,16)–15(0,15)	57.48	2.26×10^{-4}	5.16 ± 0.22	0.621			Non blended
CH_3OCHO, $v_t = 0$	130.010	11(2,10)–10(2,9)E	40.71	3.12×10^{-5}	3.36 ± 0.35	0.284			Non blended
	130.016	11(2,10)–10(2,9)A	40.70	3.12×10^{-5}	3.56 ± 0.42	0.293			Non blended
	139.565	11(2,10)–10(1,9)E	40.71	3.82×10^{-6}	3.10 ± 0.36	0.063			Non blended
	139.569	11(2,10)–10(1,9)A	40.70	3.80×10^{-6}	3.23 ± 0.28	0.081			Non blended
	141.037	12(2,11)–11(2,10)E	47.48	4.01×10^{-5}	3.72 ± 0.29	0.784	$(1.5 \pm 0.3) \times 10^{15}$ cm^{-2}	200 ± 48 K	Non blended
	141.044	12(2,11)–11(2,10)A	47.47	4.01×10^{-5}	4.22 ± 0.89	0.875			Non blended
	141.244	11(3,8)–10(3,7)E	47.77	3.87×10^{-5}	3.90 ± 0.31	0.995			Non blended
	141.260	11(3,8)–10(3,7)A	47.75	3.87×10^{-5}	4.01 ± 0.35	0.846			Non blended
	141.350	17(6,11)–17(5,12)A	114.59	4.09×10^{-6}	5.86 ± 1.09	0.199			Blended with CH_3OCH_3
	141.354	17(6,11)–17(5,12)E	114.60	3.98×10^{-6}	3.37 ± 0.50	0.054			Non blended
CH_3OCHO, $v_t = 1$	127.836	10(2,8)–9(2,7)A	223.96	2.95×10^{-5}	4.59 ± 0.78	0.102			Non blended
	128.273	10(2,8)–9(2,7)E	223.32	2.99×10^{-5}	3.96 ± 0.69	0.076			Non blended
	139.381	11(3,8)–10(3,7)A	233.19	3.70×10^{-5}	4.63 ± 0.86	0.133	$(7.1 \pm 0.5) \times 10^{14}$ cm^{-2}	196 ± 74 K	Non blended
	139.635	11(3,8)–10(3,7)E	232.67	3.72×10^{-5}	4.36 ± 0.44	0.124			Non blended
	140.020	12(2,11)–11(2,10)A	235.00	3.92×10^{-5}	4.05 ± 0.23	0.144			Non blended
	140.622	11(2,9)–10(2,5)E	230.07	3.98×10^{-5}	4.81 ± 0.73	0.253			Non blended
HC_3N, $v7 = 1$	127.680	$J = 14$–13, $l = 1e$	366.80	1.61×10^{-4}	7.22 ± 0.30	1.258	$(6.02 \pm 0.5) \times 10^{13}$ cm^{-2}	160 ± 25 K	Non blended
	127.863	$J = 14$–13, $l = 1f$	366.86	1.62×10^{-4}	6.98 ± 0.22	1.072			Non blended
HC_3N, $v7 = 2$	128.169	$J = 14$–13, $l = 0$	687.82	1.63×10^{-4}	3.61 ± 0.53	0.112	$(2.50 \pm 0.3) \times 10^{13}$ cm^{-2}	180 ± 20 K	Non blended
	128.175	$J = 14$–13, $l = 2e$	691.09	1.60×10^{-4}	3.89 ± 0.82	0.233			Non blended
	128.182	$J = 14$–13, $l = 2f$	691.10	1.60×10^{-4}	3.96 ± 0.68	0.349			Non blended
NH_2CHO	128.102	$J = 6(2,4)$–5 (2,3), F = 6–5	33.38	1.28×10^{-4}	5.20 ± 0.86	0.429	$(5.01 \pm 0.2) \times 10^{13}$ cm^{-2}	180 ± 62 K	Non blended

Notes.
[a] Frequency, transitions, E_u and A_{ij} are obtained from the LTE modeling.
[b] FWHM and $\int T_{mb} dV$ are an estimate from the Gaussian fitting over the molecular lines.
[c] Blended and non-blended effects in the observed spectral lines are verified by the LTE modeling and online molecular line list database Splatalogue.

NH_2CHO are non-blended and exhibit above 5σ significance. Using the LTE spectral modeling, the best-fit column density of NH_2CHO, based on the single transition line, is $(5.01 \pm 0.2) \times 10^{13}$ cm^{-2} with an excitation temperature of 180 ± 62 K. The fractional abundance of NH_2CHO with respect to H_2 toward IRAS 18089 is $(6.25 \pm 0.8) \times 10^{-11}$.

3.3. Spatial Distribution of Detected COMs

We create the integrated intensity maps of the non-blended transitions of C_2H_5CN, CH_3OCHO ($V_t = 0$ and $V_t = 1$), HC_3N ($v7 = 1$ and $v7 = 2$), and NH_2CHO using the CASA task `IMMOMENTS` toward IRAS 18089. The integrated intensity maps of detected COMs toward IRAS 18089 are created by integrating the spectral data cubes over carefully determined channel ranges where COMs are detected (see Figure 5). We notice that the integrated intensity maps of different COMs have a peak at the position of the continuum. From the integrated emission maps, it is clear that the emission lines of different COMs may have arisen from the extended envelope of IRAS 18089. We also estimated the emitting regions of COMs toward IRAS 18089 by fitting the two-dimensional (2D) Gaussian over the integrated intensity maps using the CASA `IMFIT` task. The deconvolved beam size of the emitting region of COMs is estimated by using the following equation,

$$\theta_S = \sqrt{\theta_{50}^2 - \theta_{\rm beam}^2}, \quad (5)$$

where $\theta_{50} = 2\sqrt{A/\pi}$ denotes the diameter of the circle with area, A is the area that encloses 50% of the peak intensity, and $\theta_{\rm beam}$ is the half-power width of the synthesized beam of the integrated emission maps (Rivilla et al. 2017). The value of θ_{50} is estimated using the task `IMFIT`. The estimated emitting regions of COMs are shown in Table 3. The emitting regions of C_2H_5CN vary between 12.″09 (29.43 pc) and 12.″12 (29.50 pc). The emitting regions of CH_3OCHO with $V_t = 0$ and $V_t = 1$ states vary between 12.″07 (29.38 pc)–12.″15 (29.57 pc) and 12.″07 (29.38 pc)–12.″14 (29.55 pc). The emitting regions of HC_3N with vibrationally excited states $v7 = 1$ and $v7 = 2$ vary between 12.″11 (29.47 pc)–12.″12 (29.50 pc) and 12.″10 (29.45 pc)–12.″11 (29.47 pc). Similarly, the emitting region of NH_2CHO is 12.″13 (29.52 pc). A smaller emitting region of COMs in comparison to the synthesized beam size implies that the emitting area of COMs is spatially unresolved in the current data set. Further high-resolution observations of these lines are required, possibly using the ALMA 12 m array, to examine the distribution and chemical morphology of COMs in the IRAS 18089 region.

4. Discussion

4.1. Possible Formation Mechanism of COMs

4.1.1. Ethyl Cyanide (C_2H_5CN)

The N-bearing molecule, C_2H_5CN, is formed on the grain surface of high-mass protostars and hot molecular cores (see Mehringer et al. 2004; Garrod 2013; Garrod et al. 2017, 2022, for details). Garrod (2013) showed that the subsequential hydrogenation of HC_3N in the freefall collapse phase can form vinyl cyanide (CH_2CHCN) ($HC_3N + 2H \rightarrow CH_2CHCN$). The subsequential hydrogenation of the CH_2CHCN forms C_2H_5CN on the grain surface of the hot molecular cores and high-mass protostars ($CH_2CHCN + 2H \rightarrow C_2H_5CN$; Garrod 2013), through barrierless and exothermic radical–radical reactions (Singh et al. 2021). This particular chemical reaction is demonstrated to be the most efficient way for the formation of C_2H_5CN toward Sgr B2, G10.47+0.03, G31.41+0.31, and other molecular cores (Belloche et al. 2009; Manna & Pal 2023; Mininni et al. 2023). This reaction may be most efficient toward IRAS 18089 because HC_3N acts as a possible precursor of C_2H_5CN, and we detected the emission lines of HC_3N from this source, which we already discussed in this paper.

4.1.2. Methyl Formate (CH_3OCHO)

In this article, we present the first detection of CH_3OCHO with $V_t = 0$ and $V_t = 1$ states toward IRAS 18089 using the ACA. In the hot molecular cores and high-mass protostars, the CH_3OCHO molecule can efficiently be formed by the reaction of CH_3O and HCO radicals on the surface of dust grains ($CH_3O + HCO \rightarrow CH_3OCHO$) (see Garrod et al. 2008, and references therein). Earlier, Manna & Pal (2022) showed that the reactions between radical CH_3O and radical HCO produce CH_3OCHO toward the hot molecular core IRAS 18566+0408. Garrod (2013) showed the chemical reaction between CH_3O and HCO is mobile between 30 and 40 K, and this chemical reaction is the most efficient pathway to the formation of CH_3OCHO toward the hot molecular cores and high-mass protostars. According to the chemical modeling of Garrod (2013), the gas phase CH_3OCHO mainly comes from the ice phase of massive protostars. Earlier, Gorai et al. (2021) reported that the UV photodissociation of CH_3OH leads to the formation of CH_2O, CH_3O, and CH_3 at around a temperature of 40 K, and these molecules create the COMs, like CH_3OCHO and CH_3OCH_3. At temperature $T \sim 40$ K in the gas phase, the reaction of protonated CH_3OH and H_2CO creates $H_5C_2O_2^+$ (Gorai et al. 2021). The CH_3OCHO is created in the hot molecular cores and massive protostars via the electron recombination of $H_5C_2O_2^+$ ($H_5C_2O_2^+ + e^- \longrightarrow CH_3OCHO + H$) (Bonfand et al. 2019; Gorai et al. 2021). Earlier, Balucani et al. (2015) proposed an efficient gas phase reaction of CH_3OCHO in a cold environment where CH_3OCH_3 behaves as a possible precursor of CH_3OCHO. Therefore, it is evident that CH_3OCHO can be produced through both grain surface and gas phase reactions in the hot molecular cores and high-mass protostars. Note that Beuther et al. (2005) detected CH_3OCH_3 with transition $J = 19(1,18)$–$18(2,17)$AA toward IRAS 18089 using SMA. However, such detection of a single transition line

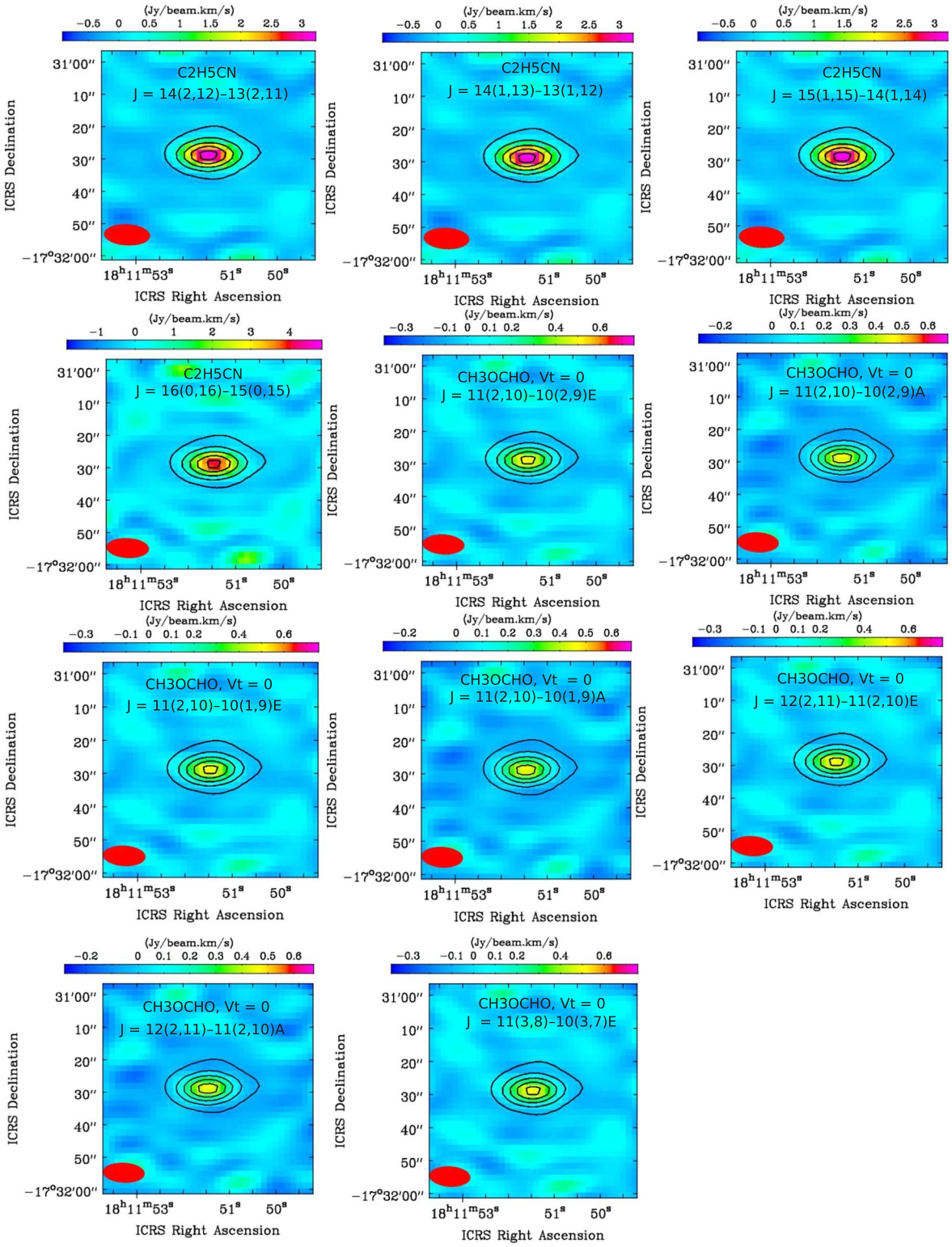

Figure 5. Integrated intensity maps of C_2H_5CN, CH_3OCHO (both $V_t = 0$ and $V_t = 1$), HC_3N (both $v7 = 1$ and $v7 = 2$), and NH_2CHO toward IRAS 18089, which are overlaid with the 2.1 mm continuum emission map of IRAS 18089 (black contours). The contour levels are at 20%, 40%, 60%, 80%, and 100% of the peak flux. The red circles represent the synthesized beam of the integrated emission maps.

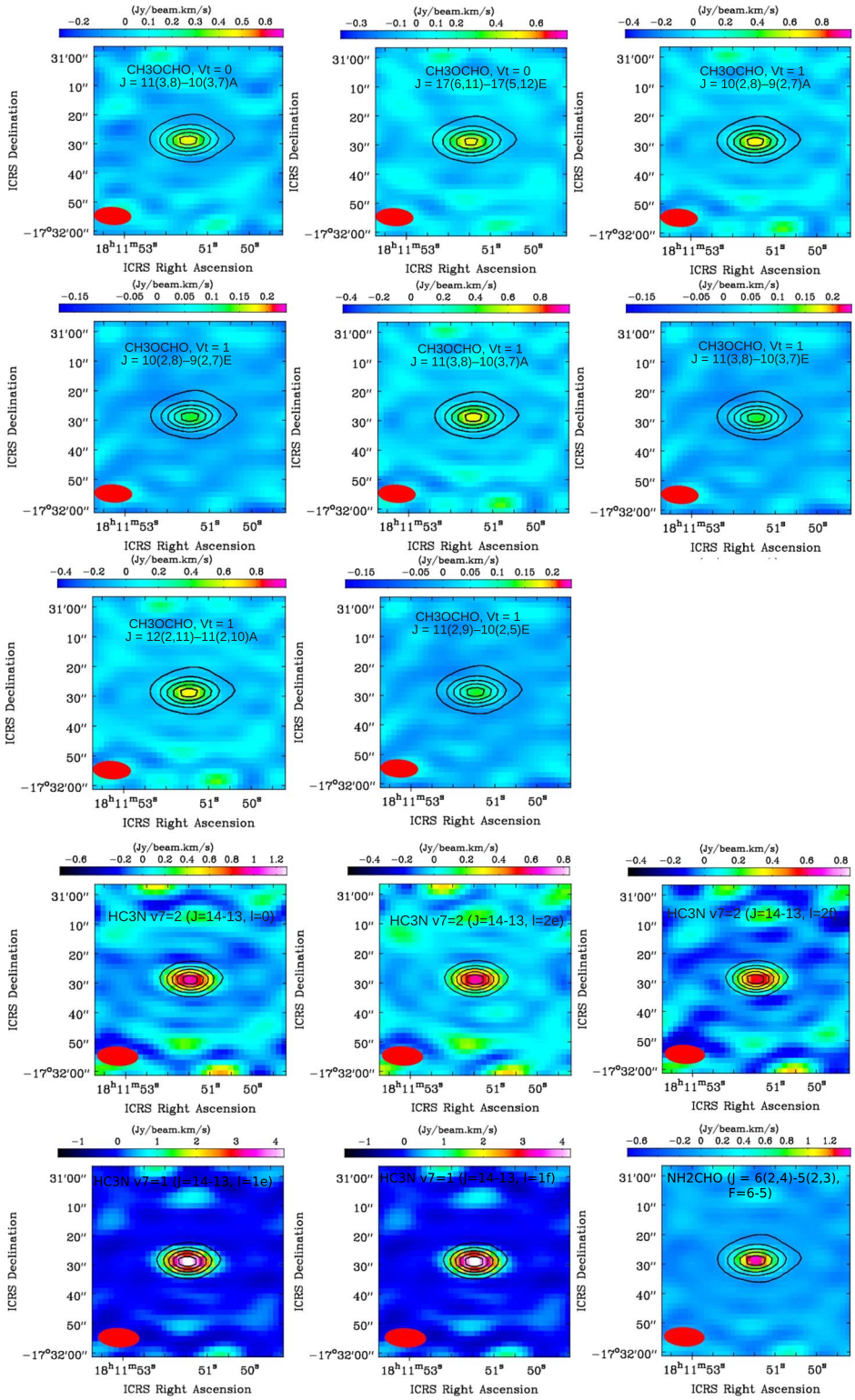

Figure 5. (Continued.)

Table 3
Estimated Emitting Regions of Detected COMs Toward IRAS 18089

Molecule	Observed Frequency (GHz)	Transition	Emitting Region (″)	Physical Scale[a] (pc)
C_2H_5CN	127.520	14(2,12)–13(2,11)	12.09 ± 0.61	29.43
	127.618	14(1,13)–13(1,12)	12.10 ± 0.65	29.45
	129.795	15(1,15)–14(1,14)	12.12 ± 0.59	29.50
	139.335	16(0,16)–15(0,15)	12.11 ± 0.60	29.47
CH_3OCHO, $v_t = 0$	130.010	11(2,10)–10(2,9)E	12.08 ± 0.58	29.40
	130.016	11(2,10)–10(2,9)A	12.07 ± 0.57	29.38
	139.565	11(2,10)–10(1,9)E	12.09 ± 0.59	29.43
	139.569	11(2,10)–10(1,9)A	12.11 ± 0.61	29.47
	141.037	12(2,11)–11(2,10)E	12.14 ± 0.58	29.55
	141.044	12(2,11)–11(2,10)A	12.09 ± 0.55	29.43
	141.244	11(3,8)–10(3,7)E	12.15 ± 0.59	29.57
	141.260	11(3,8)–10(3,7)A	12.11 ± 0.58	29.47
	141.354	17(6,11)–17(5,12)E	12.08 ± 0.61	29.40
CH_3OCHO, $v_t = 1$	127.836	10(2,8)–9(2,7)A	12.11 ± 0.58	29.48
	128.276	10(2,8)–9(2,7)E	12.10 ± 0.61	29.45
	139.381	11(3,8)–10(3,7)A	12.14 ± 0.59	29.55
	139.635	11(3,8)–10(3,7)E	12.07 ± 0.57	29.38
	140.020	12(2,11)–11(2,10)A	12.11 ± 0.60	29.47
	140.622	11(2,9)–10(2,5)E	12.09 ± 0.56	29.43
HC_3N, $v7 = 1$	127.680	$J = 14$–13, $l = 1e$	12.11 ± 0.62	29.47
	127.863	$J = 14$–13, $l = 1f$	12.12 ± 0.63	29.50
HC_3N, $v7 = 2$	128.169	$J = 14$–13, $l = 0$	12.10 ± 0.58	29.45
	128.175	$J = 14$–13, $l = 2e$	12.11 ± 0.60	29.47
	128.182	$J = 14$–13, $l = 2f$	12.10 ± 0.59	29.45
NH_2CHO	128.102	$J = 6(2,4)$–5(2,3), $F = 6$–5	12.13 ± 0.62	29.52

Note.
[a] During the estimation of the physical scale of the emitting regions of different molecules, we used the cosmological parameters from Plank with Hubble constant $H_0 = 0.6731$, $\Omega_M = 0.315$, and $\Omega_L = 0.685$ (Aghanim et al. 2020).

of one complex molecule could not be considered as conclusive evidence of the presence of the molecule in high-mass protostars.

4.1.3. Cyanoacetylene (HC_3N)

In the ISM, acetylene (C_2H_2) is one of the known compounds that is formed on the grain surfaces (Chapman et al. 2009). After the evaporation of C_2H_2 from the grains, there are two possible scenarios.

1. When the UV field is strong, like in photodissociation regions (PDRs), then C_2H_2 photodissociates into the ethynyl radical (C_2H) ($C_2H_2 + h\nu \rightarrow C_2H + H$) (Cherchneff et al. 1993; Meier & Turner 2005).

2. In the weak UV field regime (without a PDR) in the presence of the cyano radical (CN), C_2H_2 reacts with CN to create HC_3N ($C_2H_2 + CN \rightarrow HC_3N + H$) (Fukuzawa & Osamura 1997; Meier & Turner 2005; Chapman et al. 2009). Recently, Taniguchi et al. (2022) claimed that the HC_3N is created in high-mass protostars and UC H II regions when C_2H_2 immediately reacts with the CN. The HC_3N molecule is associated with highly dense, warm, and shielded gas in the star-forming regions or high-mass protostars (Taniguchi et al. 2022).

In the star-forming regions, with the presence of UV radiation, the HC_3N molecule is easily destroyed by reacting with C+ ions (Rodriguez-Franco et al. 1998; Meier & Turner 2005). After the destruction, HC_3N converts into C_2H or C_3N if HC_3N is photodissociated (Cherchneff et al. 1993). Similarly, HC_3N converts into C_3H^+ or C_4N^+ if HC_3N reacts with C+ (Bohme & Raksit 1985). The possible destruction reactions are:

$$HC_3N + h\nu \rightarrow C_2H + CN, \quad (6)$$

$$HC_3N + h\nu \rightarrow C_3N + H, \quad (7)$$

$$HC_3N + C^+ \rightarrow C_3H^+ + CN, \quad (8)$$

$$HC_3N + C^+ \rightarrow C_4N^+ + H. \quad (9)$$

The rates of the above reaction are reported in Cherchneff et al. (1993), and Taniguchi et al. (2022) showed that these

destruction pathways are the most efficient toward high-mass protostars and UC H II regions.

4.1.4. Formamide (NH_2CHO)

In the ISM, the formation pathways of NH_2CHO are still a topic of debate in both gas phase and solid state ice mantle formation routes (Garrod et al. 2008). Previously, Garrod (2013) showed that NH_2CHO is created in the gas phase barrierless reaction between NH_2 and H_2CO ($NH_2 + H_2CO \rightarrow NH_2CHO + H$). Earlier, Garrod (2013) and Suzuki et al. (2018) showed that this reaction is the most efficient for the formation of NH_2CHO toward hot molecular cores. After that, Gorai & Bhat et al. (2020) claimed that the reaction is responsible for the production of NH_2CHO toward G10.47+0.03.

4.2. Comparison between the Observed and Modeled Abundance of COMs

Here we compare the estimated fractional abundances of C_2H_5CN, CH_3OCHO, HC_3N, and NH_2CHO toward IRAS 18089 with the existing three-phase warm-up chemical model abundances of Suzuki et al. (2018). For chemical modeling, Suzuki et al. (2018) used the gas-grain chemical kinetics code NAUTILUS in the environment of hot molecular cores and massive protostars. During the chemical modeling of complex molecules, Suzuki et al. (2018) assumed an isothermal collapse phase after a static warm-up phase. In the first phase, the gas density increases from 3×10^3 to $2 \times 10^7\,cm^{-3}$ and dust temperature decreases from 16 to 8 K under the freefall collapse (Suzuki et al. 2018). In the second phase, known as the warm-up phase, the dust temperature increases from 8 to 400 K, and the gas density remains fixed at $2 \times 10^7\,cm^{-3}$. For the chemical modeling, Suzuki et al. (2018) used the following reactions on the grain surfaces to produce the C_2H_5CN, CH_3OCHO, and HC_3N:

$$CH_2CHCN + 2H \rightarrow C_2H_5CN, \quad (10)$$

$$CH_3O + HCO \rightarrow CH_3OCHO, \quad (11)$$

$$C_2H_2 + CN \rightarrow HC_3N + H, \quad (12)$$

$$NH_2 + H_2CO \rightarrow NH_2CHO + H. \quad (13)$$

We explain reactions (10), (11), (12), and (13) in Section 4.1. The three-phase warm-up chemical modeling of Suzuki et al. (2018) is appropriate for explaining the chemical abundance and evolution of COMs toward IRAS 18089 because the gas density of IRAS 18089 is $1.3 \times 10^7\,cm^{-3}$ (Sanhueza et al. 2021) and the gas temperature is above 100 K (Beuther et al. 2004a). After the chemical modeling, Suzuki et al. (2018) determined the modeled abundance of C_2H_5CN, CH_3OCHO, HC_3N, and NH_2CHO to be 6.3×10^{-10}, 4.9×10^{-9}, 1.1×10^{-11}, and 4.0×10^{-11} respectively using the fast warm-up model with the help of reactions (10), (11), (12), and (13) on the grain surfaces and gas phases of hot molecular cores and massive prostars. Our estimated abundances of C_2H_5CN, CH_3OCHO ($V_t = 0$), HC_3N, and NH_2CHO are reported in Section 3.2. We find that our estimated abundances of C_2H_5CN, CH_3OCHO, HC_3N, and NH_2CHO are quite similar to the chemical modeling abundances of Suzuki et al. (2018). This result indicates that reactions (10), (11), (12), and (13) may be responsible for the production of C_2H_5CN, CH_3OCHO, HC_3N, and NH_2CHO toward IRAS 18089.

5. Conclusion

In this article, we present the identification of the rotational emission lines of C_2H_5CN, CH_3OCHO ($V_t = 0$ and $V_t = 1$), HC_3N ($v7 = 1$ and $v7 = 2$), and NH_2CHO toward IRAS 18089. The estimated abundance of C_2H_5CN toward IRAS 18089 is $(1.40 \pm 0.5) \times 10^{-10}$. The estimated abundance of CH_3OCHO with respect to H_2 is $(1.90 \pm 0.9) \times 10^{-9}$ and $(8.90 \pm 0.8) \times 10^{-10}$ for $V_t = 0$ and $V_t = 1$, respectively. The abundance of HC_3N toward IRAS 18089 is $(7.5 \pm 0.7) \times 10^{-11}$ (for $v7 = 1$) and $(3.1 \pm 0.4) \times 10^{-11}$ (for $v7 = 2$). Similarly, the abundance of NH_2CHO toward IRAS 18089 is $(6.25 \pm 0.8) \times 10^{-11}$. We created the integrated emission maps of detected COMs, and we observed that the detected emission lines of different COMs arise from the extended envelope of the protostar. We also compared the estimated abundances of C_2H_5CN, CH_3OCHO, HC_3N, and NH_2CHO with the existing three-phase warm-up modeling abundances of those molecules. After the comparisons, we noticed that the observed and modeled abundances are quite similar. So, the N-bearing molecules C_2H_5CN and HC_3N are most probably created via the subsequential hydrogenation of CH_2CHCN and the reactions between C_2H_2 and CN on the grain surface of IRAS 18089. The O-bearing molecule CH_3OCHO is probably created via the reactions between radical CH_3O and radical HCO on the grain surface of IRAS 18089. Similarly, the O- and N-bearing molecule NH_2CHO is most probably formed between the reactions of NH_2 and H_2CO in the gas phase of IRAS 18089. The prebiotic chemistry of C_2H_5CN, CH_3OCHO, HC_3N, and NH_2CHO toward IRAS 18089 suggests that both gas phase and grain surface chemistry are efficient for the production of other COMs in that protostar, including those molecules that are chemically connected with those detected molecules. The detections of both N- and O-bearing molecules toward IRAS 18089 indicate that IRAS 18089 is a reservoir of several other COMs. A spectral line survey is needed using the ALMA 12 m array to understand the prebiotic chemistry in this high-mass protostar, which will be carried out in our follow-up study.

Acknowledgments

We thank the anonymous referee for the helpful comments that improved the manuscript. A.M. acknowledges the Swami Vivekananda Merit-cum-Means Scholarship (SVMCM) for financial support for this research. This paper makes use of the

following ALMA data: ADS /JAO.ALMA#2016.2.00005.S. ALMA is a partnership of ESO (representing its member states), NSF (USA), and NINS (Japan), together with NRC (Canada), MOST and ASIAA (Taiwan, China), and KASI (Republic of Korea), in cooperation with the Republic of Chile. The Joint ALMA Observatory is operated by ESO, AUI/NRAO, and NAOJ.

Conflicts of Interest

The authors declare no conflict of interest.

ORCID iDs

Arijit Manna https://orcid.org/0000-0001-9133-3465
Sabyasachi Pal https://orcid.org/0000-0003-2325-8509
Tapas Baug https://orcid.org/0000-0003-0295-6586

References

Aghanim, N., Akrami, Y., Ashdown, M., et al. 2020, A&A, 641, 67
Andron, I., Gratier, P., Majumdar, L., et al. 2018, MNRAS, 481, 5651
Balucani, N., Ceccarelli, C., & Taquet, V. 2015, MNRAS, 449, L16
Belloche, A., Garrod, R. T., Müller, H. S. P., et al. 2009, A&A, 499, 215
Belloche, A., Müller, H. S. P., Menten, K. M., Schilke, P., & Comito, C. 2013, A&A, 559, A47
Beuther, H., Hunter, T. R., Zhang, Q., et al. 2004a, ApJL, 616, L23
Beuther, H., Schilke, P., Menten, K. M., et al. 2002a, ApJ, 566, 945
Beuther, H., Vlemmings, W. H. T., Rao, R., & van der Tak, F. F. S. 2010, ApJL, 724, L113
Beuther, H., Walsh, A., Schilke, P., et al. 2002b, A&A, 390, 289
Beuther, H., Zhang, Q., Greenhill, L. J., et al. 2005, ApJ, 632, 355
Beuther, H., Zhang, Q., Hunter, T. R., et al. 2004b, ApJL, 616, L19
Beuther, H., Zhang, Q., Sridharan, T. K., & Chen, Y. 2005, ApJ, 628, 800
Bohme, D. K., & Raksit, A. B. 1985, MNRAS, 213, 717
Bonfand, M., Belloche, A., Garrod, R. T., et al. 2019, A&A, 628, A27
Bruderer, S., Benz, A. O., Doty, S. D., van Dishoeck, E. F., & Bourke, T. L. 2009, ApJ, 700, 872
Bruderer, S., Benz, A. O., Stäuber, P., & Doty, S. D. 2010, ApJ, 720, 1432
Calcutt, H., Jørgensen, J. K., Müller, H. S. P., et al. 2018, A&A, 616, A90
Caselli, P., & Ceccarelli, C. 2012, A&ARv, 20, 56
Cazaux, S., Tielens, A. G. G. M., Ceccarelli, C., et al. 2003, ApJL, 593, L151
Chapman, J. F., Millar, T. J., Wardle, M., Burton, M. G., & Walsh, A. J. 2009, MNRAS, 394, 221
Charnley, S. B., Tielens, A. G. G. M., & Millar, T. J. 1992, ApJL, 399, L71
Cherchneff, I., Glassgold, A. E., & Mamon, G. A. 1993, ApJ, 410, 188
Chini, R., Hoffmeister, V., Kimeswenger, S., et al. 2004, Nature, 429, 155
Cox, A. N., & Pilachowski, C. A. 2000, PhT, 53, 77
de Wit, W. J., Testi, L., Palla, F., & Zinnecker, H. 2005, A&A, 437, 247
Evans, N. J., II, Di Francesco, J., Lee, J.-E., et al. 2015, ApJ, 814, 22
Fukuzawa, K., & Osamura, Y. 1997, ApJ, 489, 113
Garrod, R. T. 2013, ApJS, 765, 60
Garrod, R. T., Belloche, A., Müller, H. S. P., & Menten, K. M. 2017, A&A, 601, A48
Garrod, R. T., & Herbst, E. 2006, A&A, 457, 927
Garrod, R. T., Jin, M., Matis, K. A., et al. 2022, ApJS, 259, 1
Garrod, R. T., Weaver, S. L. W., & Herbst, E. 2008, ApJ, 682, 283
Gorai, P., Bhat, B., et al. 2020, ApJ, 895, 86
Gorai, P., Das, A., Shimonishi, T., et al. 2021, ApJ, 907, 108
Hanwell, M. D., Curtis, D. E., Lonie, D. C., et al. 2012, J. Cheminform, 4, 17
Herbst, E., & van Dishoeck, E. F. 2009, ARA&A, 47, 427
Isokoski, K., Bottinelli, S., & van Dishoeck, E. F. 2013, A&A, 554, A100
Jørgensen, J. K., van der Wiel, M. H. D., Coutens, A., et al. 2016, A&A, 595, A117
Liu, H.-L., Liu, T., Evans, N. J., et al. 2021, MNRAS, 505, 2801
Liu, T., Evans, N. J., Kim, K. T., et al. 2020, MNRAS, 496, 2790
Manna, A., & Pal, S. 2022, Ap&SS, 367, 94
Manna, A., & Pal, S. 2023, Ap&SS, 368, 44
Manna, A., & Pal, S. 2024, ESC, 8, 665
McMullin, J. P., Waters, B., Schiebel, D., Young, W., & Golap, K. 2007, in ASP Conf Ser. 376, Astronomical Data Analysis Software and Systems XVI, ed. R. A. Shaw, F. Hill, & D. J. Bell (San Francisco, CA: ASP), 127
Mehringer, D. M., Pearson, J. C., Keene, J., & Phillips, T. G. 2004, ApJ, 608, 306
Meier, D. S., & Turner, J. L. 2005, ApJ, 618, 259
Millar, T. J., Herbst, E., & Charnley, S. B. 1991, ApJ, 369, 147
Mininni, C., Beltrán, M. T., Colzi, L., et al. 2023, A&A, 677, A15
Mondal, S. K., Gorai, P., Sil, M., et al. 2021, ApJ, 922, 194
Mondal, S. K., Iqbal, W., Gorai, P., et al. 2023, A&A, 669, A71
Motogi, K., Hirota, T., Machida, M. N., et al. 2019, ApJL, 877, L25
Müller, H. S. P., SchlMöder, F., Stutzki, J., & Winnewisser, G. 2005, JMoSt, 742, 215
Öberg, K. I., Garrod, R. T., van Dishoeck, E. F., & Linnartz, H. 2009, A&A, 504, 891
Perley, R. A., & Butler, B. J. 2017, ApJs, 230, 1538
Pestalozzi, M. R., Elitzur, M., Conway, J. E., & Booth, R. S. 2004, ApJL, 603, L113
Qin, S.-L., Liu, T., Liu, X., et al. 2022, MNRAS, 511, 3463
Rivilla, V. M., Beltrán, M. T., Cesaroni, R., et al. 2017, A&A, 598, A59
Rodriguez-Franco, A., Martin-Pintado, J., & Fuente, A. 1998, A&A, 329, 1097
Sakai, N., Sakai, T., Hirota, T., et al. 2008, ApJ, 672, 371
Sakai, N., & Yamamoto, S. 2013, ChRv, 113, 8981
Sanhueza, P., Girart, J. M., Padovani, M., et al. 2021, ApJL, 1, L10
Shepherd, D. S., Yu, K. C., Bally, J., & Testi, L. 2000, ApJ, 535, 833
Singh, K. K., Tandon, P., Misra, A., et al. 2021, IJAsB, 20, 62
Sridharan, T. K., Beuther, H., Schilke, P., Menten, K. M., & Wyrowski, F. 2002, ApJ, 566, 931
Suzuki, T., Majumdar, L., & Ohishi, M. 2018, ApJ, 863, 51
Taniguchi, K., Tanaka, K. E. I., Zhang, Y., et al. 2022, APJ, 931, 99
Tielens, A. G. G. M., & Charnley, S. B. 1997, Origins Life Evol. Biosphere, 27, 23
Tielens, A. G. G. M., & Hagen, W. 1982, A&A, 114, 245
Torrelles, J. M., Gomez, J. F., Rodriguez, L. F., et al. 1996, ApJL, 457, L107
Tudorie, M., Ilyushin, V., vander Auwera, J., et al. 2012, JCP, 137, 064304
van Dishoeck, E. F., & Blake, G. A. 1998, ARA&A, 36, 317
Vastel, C., Bottinelli, S., Caux, E., Glorian, J.-M., & Boiziot, M. 2015, in Proc. Annual Meeting of the French Society of Astronomy and Astrophysics, ed. F. Martins et al. (Toulouse: French Society of Astronomy and Astrophysics), 313
Whittet, D. C. B. 1992, JBAA, 102, 230
Xu, Y., Moscadelli, L., Reid, M. J., et al. 2011, ApJ, 733, 25
Zapata, L. A., Rodríguez, L. F., Ho, P. T. P., et al. 2006, AJ, 131, 939